

Turbulence in Continental Stratocumulus, Part I: External Forcings and Turbulence Structures

Ming Fang · Bruce A. Albrecht · Virendra P. Ghate ·
Pavlos Kollias

Received: 3 December 2012 / Accepted: 15 October 2013
© Springer Science+Business Media Dordrecht 2013

Abstract Comprehensive, ground-based observations from the US Department of Energy Atmospheric Radiation Measurements program Southern Great Plains site are used to study the variability of turbulence forcings and cloud-scale turbulence structures in a continental stratocumulus cloud. The turbulence observations are made from an upward facing cloud (35 GHz) Doppler radar. Cloud base and liquid water path are characterized using a lidar at the surface and a microwave radiometer. The turbulence characterizations are compared and contrasted with those observed in marine stratocumulus clouds. During the 16-h observation period used in this study the cloud-base and cloud-top heights evolve with time and changes in liquid water path observed by the radiometer are consistent with variations in cloud depth. Unlike marine stratocumulus clouds, a diurnal cycle of cloud thickness and liquid water path is not observed. The observed surface latent, sensible, and virtual sensible heat fluxes and the radiative fluxes exhibit a diurnal cycle with values increasing from sunrise to afternoon and decreasing afterwards. During the night, the sensible heat, virtual sensible heat and the net radiative fluxes at the surface are slightly negative. Solar radiative heating prevails in the cloud layer during the day and strong radiative cooling exists at cloud top even during the day. Unlike marine stratocumulus, surface heating described by the convective velocity scale W_s^* and cloud-top cooling described by W_r^* are both important in driving the in-cloud turbulence during the day, whereas cloud-top cooling is the exclusive contributor during the night. The combined W_s^* and W_r^* (the total velocity scale W_t^*) provides a useful way to track the evolution of the turbulence structure in the cloud. The variance of the radar-measured radial

M. Fang (✉) · B. A. Albrecht
Rosenstiel School of Marine and Atmospheric Science, The University of Miami,
4600 Rickenbacker Causeway, Miami, FL 33149, USA
e-mail: mfang3219@hotmail.com; mfang@rsmas.miami.edu

V. P. Ghate
Division of Environmental Sciences, Argonne National Laboratory,
9700 S. Cass Ave, Argonne, IL, USA

P. Kollias
Department of Atmospheric and Oceanic Sciences, McGill University, Montreal, QC, Canada

velocity, which is related to resolved turbulence, follows the diurnal cycle and is consistent with the total velocity scale W_t^* variations. It is higher during the day and lower during the night, which is contrary to that in marine stratocumulus. The W_t^* values are lowest around sunset when the radiative cooling is also small due to upper-level clouds observed above the low-level stratus. The vertical distribution of the variance results from the surface heating during the day and cloud-top cooling during the night. The squared spectrum width, which is related to turbulence structures within the radar sampling volume (unresolved turbulence) also follows the diurnal cycle. Its vertical distribution indicates that the unresolved turbulence more closely relates to the processes near cloud top. Turbulence in the cloud requires about an hour to respond to the external forcings of surface heating and cloud-top radiative cooling. Positive skewness prevails during the day and negative skewness prevails at night with a sharp transition around sunset. Resolved turbulence dominates near cloud base whereas unresolved turbulence dominates near cloud top. The turbulence characteristics and variability defined in this study can be used to evaluate the time evolution of turbulence structures in large eddy simulation forced by surface and cloud-top radiative forcings.

Keywords Continental stratocumulus · External forcings · Turbulence

1 Introduction

Continental stratocumulus clouds are frequently observed in the cold side of mid-latitude frontal systems or in association with anticyclones. They can affect the local surface temperature and the energy and water budget as well as the local climate. Despite their possible role in modulating overland surface energy and moisture budgets, they have received relatively little attention (Kollias and Albrecht 2000; Zhu et al. 2001; Ghate et al. 2010; Mechem et al. 2010) compared with their marine stratocumulus counterparts that persist in subsidence areas over the subtropical oceans (Wood 2012).

Turbulence is one of the most important physical processes in the atmospheric boundary layer. Large eddies with a scale comparable with the boundary-layer depth can transport energy, water vapour, momentum and pollutants whereas small-scale turbulence can influence the cloud structure and cloud droplet growth (e.g., East and Marshall 1954; Jonas 1996; Wang and Grabowski 2009; Xue et al. 2008). Furthermore, turbulence and associated fluxes can affect supersaturation, mixing and entrainment and therefore are critical to the formation, maintenance and dissipation of stratocumulus clouds. Over land, the surface heating is an external forcing that can generate turbulence as well as the surface friction. In addition, in the cloud-topped boundary layer, cloud-top radiative cooling is another mechanism that can drive turbulence (Lilly 1968; Kollias and Albrecht 2000; Mechem et al. 2010). However, our knowledge of the turbulence structure and relative importance between surface heating and cloud-top cooling in the turbulence generation in continental stratocumulus clouds is still limited. The detailed analysis of boundary-layer cloud cases and associated turbulence can improve our understanding of not only the cloud dynamics but also cloud microphysical parameters, such as cloud-drop size distribution. This improved understanding can lead to an improved representation of stratocumulus clouds in numerical weather prediction and global climate models (Boutle and Abel 2012).

Here, observations from the US Department of Energy Atmospheric Radiation Measurement program millimetre-wave cloud radar (Moran et al. 1998) and other ancillary instruments combined with the fields from a radiative transfer model are used to examine the

turbulence structure and forcing associated with 16 consecutive hours of stratocumulus observations over the Southern Great Plains site.

[Frisch et al. \(1995\)](#) were the first to use the cloud radar to study turbulence in stratocumulus clouds. Compared with aircraft measurements, profiling radar measurements provide a means to study the vertical structure of the flow in clouds in detail that aircraft measurements cannot make, since the aircraft measurements cannot be made at such a fine vertical resolution. Further, since the observations from a single aircraft cannot be made simultaneously at different heights, the temporal evolution of the vertical structure of the turbulence is difficult to characterize. After the pioneering work of [Frisch et al. \(1995\)](#), other investigators have used surface-based radar observations to examine the turbulence structure of continental stratocumulus clouds (e.g. [Kollias et al. 2001](#); [Ghate et al. 2010](#); [Mechem et al. 2010](#); [Sassen et al. 1999](#)). Previous studies focused on the exploitation of the variance and skewness of the mean Doppler velocity—the first moment of the Doppler spectrum to characterize the in-cloud turbulence. The primary contribution to these statistics comes from the resolved turbulence with scales larger than radar beam size. This study also uses the statistics associated with mean Doppler velocity, but the millimetre-wave cloud radar observations have a very high spatial (45 m) and temporal resolution (4 s) and therefore allow us to examine the detailed spatial structure and time evolution of the turbulence under a range of forcing conditions. Furthermore, this study uses the spectrum width, the square root of the second moment of the Doppler spectrum as well. The spectrum width also contains turbulence information, but it primarily relates to the unresolved or subscale turbulence whose scale is comparable or smaller than the radar beam size. The subgrid-scale turbulence more closely relates to the microphysics in clouds and parametrized in large-eddy simulations (LES).

This paper is the first of a two-part study and examines the relationships between turbulence generation processes due to cloud-top cooling and surface buoyancy fluxes and explores the association between the time evolution of the forcings and the time evolution of turbulence that includes both the large-eddy circulations in the clouds and the fine-scale turbulence in the inertial sub-range. The next section (Sect. 2) will introduce the instrumentation and data used in this study. Section 3 presents the meteorological background, while Sect. 4 addresses various flux and external forcings. Section 5 discusses velocity scales, and Sect. 6 includes the time evolution of the structures of variance, squared spectrum width and skewness. Section 7 represents the resolved and unresolved turbulence and the summary is given in Sect. 8. In Part II, the turbulence dissipation rates will be estimated from the spectrum width and the observed large-eddy coherent structures and their evolution analyzed.

2 Instrumentation and Data

The US Department of Energy Atmospheric Radiation Measurement program Climate Research Facility at the Southern Great Plains site at Lamont, Oklahoma was established in 1992. The heavily instrumented central facility at this site includes a profiling millimetre-wave cloud radar operating at 35 GHz. It was deployed in 1996 ([Moran et al. 1998](#)). Its digital processor, sampling strategy and data processing algorithms were updated in 2006 ([Kollias et al. 2007](#)). The millimetre-wave cloud radar can continuously collect data and is one of the primary facilities used to investigate the cloud properties and is a central piece of this study. It operates at four different modes: boundary (BL), general (GE), cirrus (CI) and precipitation (PR). The operation sequence of mode is:

BL GE BL CI BL GE BL PR/PO

where PO denotes a polarization mode. In BL mode, the millimetre-wave cloud radar has a 45-m range resolution and 1.04-s dwell time. The cycle from one BL to the next is about 4 s (Kollias et al. 2007). The one-way half power beam width of the radar is 0.2° (millimetre-wave cloud radar handbook, http://www.arm.gov/publications/techreports/handbooks/mmcr_handbook.pdf?id=71).

In addition to the millimetre-wave cloud radar, measurements from three other remote sensing instruments are used in this study. These include the ground-based micro-pulse lidar operating at 532 nm, the radar wind profiler/radio acoustic sounding system operating at 915-MHz and 1290-MHz frequencies and a microwave radiometer. These instruments are collocated with the millimetre-wave cloud radar to observe simultaneously the atmospheric column over the facility. The ground-based micro-pulse lidar can detect the height of the liquid cloud base. The millimetre-wave cloud radar detected echoes below the lidar-defined cloud base are considered as insect echoes and removed. No precipitation or virga was observed by the millimetre-wave cloud radar for the studied case. To ensure the quality of the Doppler spectrum width estimates, all data observed by millimetre-wave cloud radar with signal-to-noise ratio below -10 dB are removed too. The radar wind profiler/radio acoustic sounding system provides wind profiles between 0.1 and 5 km and virtual temperature profiles between 0.1 and 2.5 km. This study uses the wind profiles only to determine the horizontal advection wind speed needed to transfer the power spectra of the vertical velocity from frequency domain to wavenumber domain at the level of the radar gates. The microwave radiometer observes the sky brightness temperature at 23.8 and 31.4 GHz, and the liquid water path (LWP) is then calculated from these brightness temperatures (Turner et al. 2007; Ghate 2009).

The surface sensible and latent heat fluxes presented herein are observed by the eddy-correlation flux measurement system that was installed at the Atmospheric Radiation Measurement program Southern Great Plains site and provides in situ, half-hour flux estimates. The shortwave and longwave downwelling and upwelling radiative fluxes at the surface are observed by the Solar Infrared Radiation Station that was installed at the same location and provides 5-min averaged values.

The cloud evolution during the 16-h period of observations of the stratocumulus cloud shown in Fig. 1 extends from 0900 CST on 25 March 2005 to 0100 CST on 26 March 2005. For this day sunrise is at 0626 CST and sunset is at 1846 CST. Both Fig. 1a, b shows the evolution of reflectivity factor, but Fig. 1a shows the height up to 10 km so that the middle and high level clouds can be displayed too. Figure 1b–d shows only the low-level stratocumulus clouds, because they are the focus of this study. The low-level stratocumulus clouds persist during the entire 16-h observation time period. There are two horizontal dotted lines in Fig. 1a. The lower one near 2.5 km is the freezing level. The upper line near 4.6 km is the height of the -16°C isotherm that is used in the radiative transfer model to separate ice-phase clouds from mixed-phase clouds (Dunn et al. 2011). The mid-level clouds appear in four major time periods each of which is marked by two vertical dotted lines and a double arrow line. The influence of the ice-phase and mixed-phase clouds on the radiation budget of the cloud will be discussed later. The radar reflectivity values in the cloud layer are generally low (below -20 dBZ) indicating the absence of drizzle sized particles. This lack of drizzle is also evident from the absence of millimetre-wave cloud radar echoes (except for a few non-meteorological echoes due to insects in Fig. 1a) below the cloud-base height indicated by the black line in Fig. 1b. The cloud depth is about 400 m and shows some variability. The cloud top gradually increases from about 800 to 1,200 m during the observing period. A thinning of the cloud due mostly to a decrease in the cloud-top height is observed from 1900 to 2000 CST as thick upper-level clouds are observed above the low cloud. This corresponds

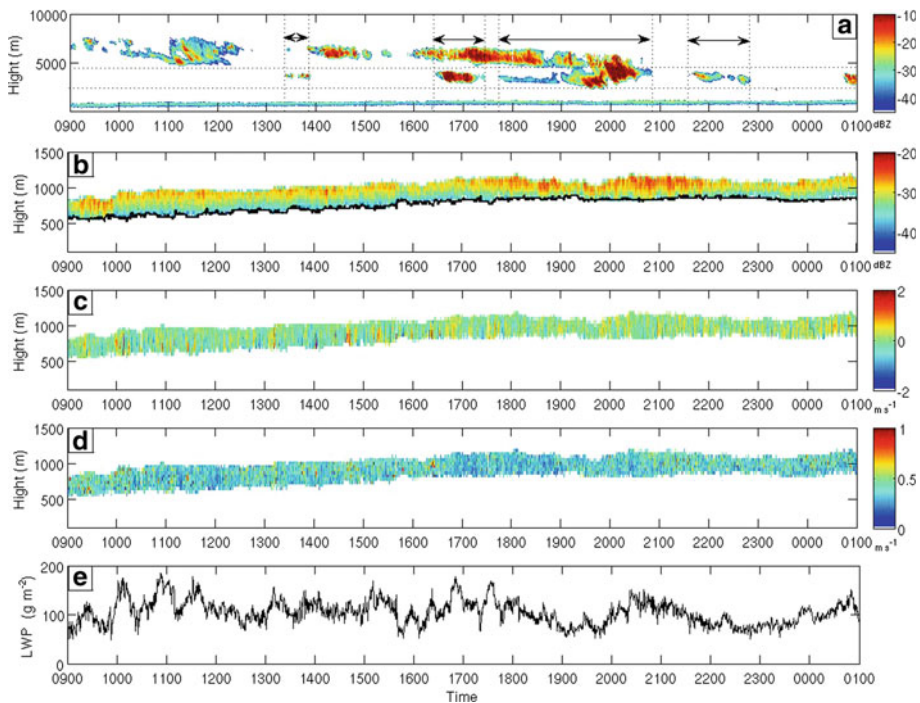


Fig. 1 The time-height display of, from *top to bottom*, reflectivity factor (**a**), reflectivity factor (**b**), radial velocity (**c**) and spectrum width (**d**) recorded by the millimetre-wave cloud radar and LWP (**e**) from the microwave radiometer. In **a**, a *double arrow lines* combined with two *vertical dotted lines* indicate a major time periods when midlevel clouds are present. The *upper horizontal dotted line* indicates -16°C height whereas the *lower one* indicates the freezing level. The *black line* in **b** is the cloud base determined from the ground-based micro-pulse lidar measurements

well with a dip in the LWP observations. The longwave radiation from thick upper-level clouds weakens the cloud-top radiative cooling that sustains and maintains the clouds, which is consistent with the thinning of the cloud layer.

Generally speaking, the time evolution of LWP is consistent with that of the cloud depth. During the first 4 h of observations there are oscillations in the LWP with a period of about 1 h. There are corresponding variations in the net shortwave differences at the surface. The mean Doppler velocity field exhibits several vertical air motion coherent structures extending from the cloud base to the cloud top; the Doppler spectrum width has values between 0.1 and 0.8 m s^{-1} .

It is well known that in marine stratocumulus clouds the cloud thickness reaches a maximum in early morning and minimum in afternoon; the variation of LWP is in phase with the cloud thickness (Wood et al. 2002; Duynkerke et al. 2004; Simon et al. 2012). However these diurnal variations are not observed in the continental stratocumulus clouds shown in Fig. 1.

3 Meteorological Conditions

The observations shown in Fig. 1 were collected following the passage of a cold front with surface winds from the north associated with an anticyclone ($1,027\text{ hPa}$) located about $1,200$

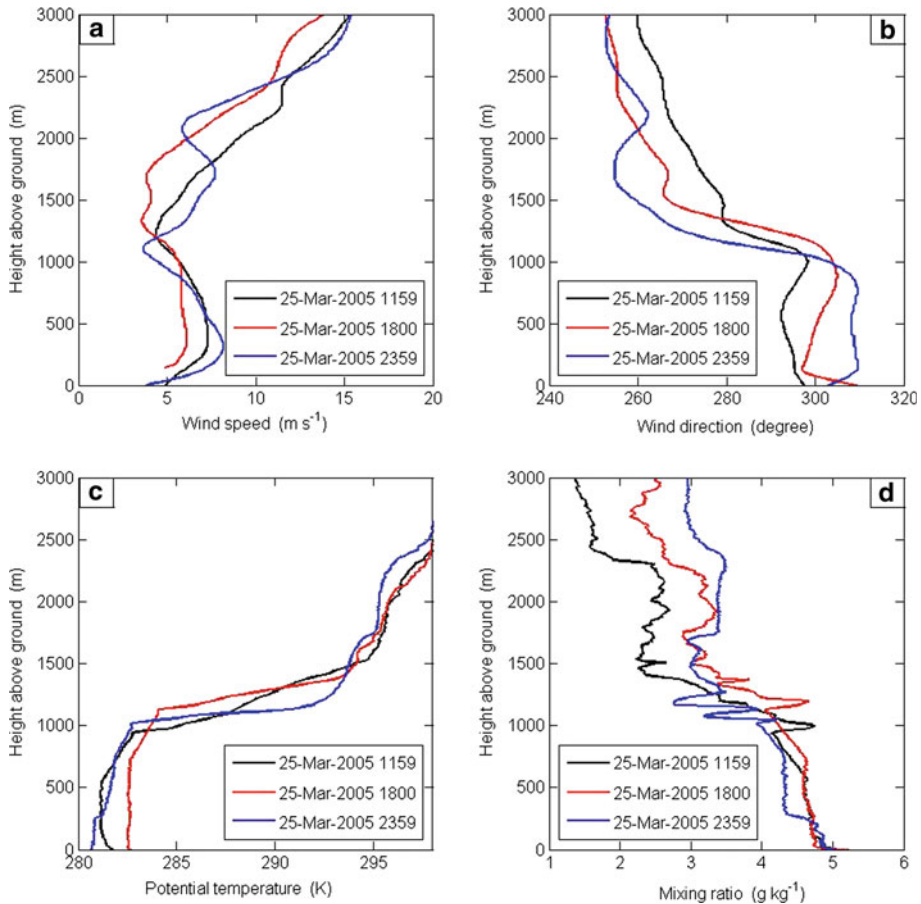


Fig. 2 Profiles of horizontal wind speed (a), wind direction (b), potential temperature (c) and mixing ratio (d) at 1200 CST (black) 1800 CST (red) and 2400 (blue) on 25 March 2005

km to the north of the observation site. Thus, the investigated stratocumulus clouds at the top of the boundary layer are associated with large-scale subsidence in the free atmosphere. This large-scale background circulation is similar to that commonly associated with marine stratocumulus clouds. [Zhu et al. \(2010\)](#) provide a full discussion of the meteorological conditions for this case for the period 0200–1600 CST on 25 March 2005.

The profiles of wind speed and direction from the radiosondes launched during the event at around 1200, 1800, and 2400 CST on 25 March 2005 are shown in Fig. 2a, b. In the 1200 CST sounding, the wind speed near the surface is about 5 m s^{-1} and increases to about 7 m s^{-1} at 400 m and decreases to about 4 m s^{-1} at the top of the boundary layer. The wind speed increases nearly linearly with height in the free atmosphere. The winds at 1800 CST are slightly weaker and nearly constant between 300 and 1,000 m. The profile at 2400 CST has a wind maximum of about 8.5 m s^{-1} at 300 m and a second maximum of 8 m s^{-1} at 1,750 m, which is above the boundary layer. The wind speed continues to increase above 2100 m, but in general the vertical shear of the horizontal wind speeds is relatively small throughout the boundary layer and near cloud top.

The wind directions in all soundings are roughly northerly within the boundary layer, but shift sharply to westerly above cloud top. Since the tops of the studied clouds are always below about 1,300 m, profiles only to 3 km are shown.

The profiles of potential temperature and mixing ratio obtained around 1200, 1800, and 2400 CST on 25 March 2005 are shown in Fig. 2c and d respectively. A sharp inversion with a strength of about 10 °C at cloud and boundary-layer top at about 1 km is indicated by the potential temperature profiles. The nearly moist adiabatic lapse rate inside cloud layer can also be observed in all three soundings. An unstable layer is indicated in the lowest 200 m of the 1200 CST sounding due to surface heating. The 1800 CST shows a classic stratocumulus-topped boundary-layer structure with a well-developed mixed layer below 700 m and air for this evening sounding is warmer than at the other times. There are two mixed layers present in the 2400 CST sounding that are decoupled. The lower one extends from the surface to 250 m and has a lower temperature compared with the one above because of the surface cooling during the night. Shown in Fig. 2d are profiles of mixing ratio. A surface layer is present in all three soundings. The 1200 CST and 1800 CST soundings have a well-mixed structure below 700 m. The 2400 CST sounding shows the two decoupled mixed layers similar to those observed in the potential temperature profile. The height of cloud top and cloud base and cloud-layer depth at the time of the soundings can be inferred from either the potential temperature profiles or the mixing ratio profiles. In the 1200 CST sounding, the cloud top and base are at about 1,000 and 570 m respectively with a cloud depth of about 430 m. In the 1800 CST sounding, the cloud top has risen to 1,200 m and the cloud base has risen to about 720 m with an approximate 480 m cloud depth. By 2400 CST, the cloud top descends to 1,020 m and the cloud depth is reduced to about 240 m. These exhibited changes in the soundings are consistent with the cloud structure from the radar and lidar observations shown in Fig. 1. A further description of the meteorological conditions for this case can be found in [Zhu et al. \(2010\)](#) and [Ghate et al. \(2010\)](#).

4 Fluxes

The buoyancy fluxes originating from surface heating and the cloud-top radiative cooling are the external forcings that drive the turbulence in the cloud and the boundary layer. Their relevant velocity scales can be used to define the intensities of the forcings and their contributions to the turbulence.

4.1 Surface Fluxes

The time series of observed latent, sensible heat and virtual sensible heat fluxes and net radiative flux at the surface are shown in Fig. 3. All these fluxes exhibit a strong diurnal cycle. The net radiative surface flux (net shortwave flux minus the net longwave flux) is positive during the day and reflects the incidence of solar radiation (transmitted through the cloud) on the surface. This flux increases from about 140 W m⁻² at 0900 CST to the maximum value about 300 W m⁻² around noon. It decreases afterwards and diminishes to zero and becomes slightly negative after sunset. During the day, the net radiative flux drives the turbulence that transports sensible and latent heat from the surface. From the energy conservation point of view, the net radiative energy warms the surface. This warming gives rise to the positive sensible and latent heat fluxes from the surface. The virtual sensible heat flux drives the production of turbulence by buoyancy effects.

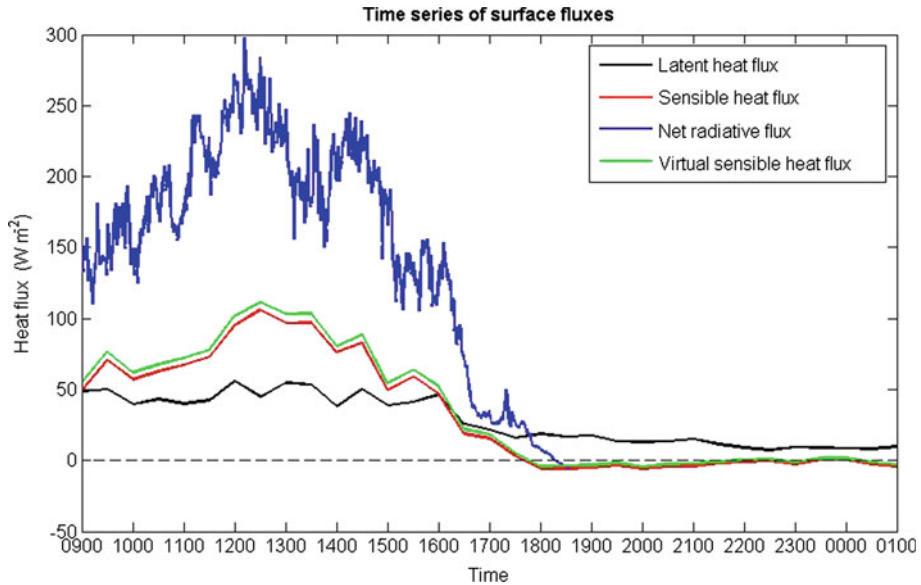


Fig. 3 Time series of latent heat flux, sensible heat flux, net radiative flux and virtual sensible heat flux at surface. The dashed line is a reference line with $y = 0$

The latent heat flux is nearly a constant fluctuating around 50 W m^{-2} from 0900 CST to 1600 CST, and then decreases to a minimum of about 20 W m^{-2} at 0100 CST on 26 March 2005. The virtual sensible heat flux increases from about 60 W m^{-2} at 0900 CST to a maximum of about 110 W m^{-2} around noon, and then decreases and diminishes to zero and is slightly negative after sunset. After 1620 CST, the virtual sensible heat flux decreases below the latent heat flux. This indicates that the air temperature is higher than surface temperature and there is a sensible heat transport from the air to the surface. The slightly negative values of the sensible heat flux after 1800 CST confirm this observation. The slightly positive values of the heat flux around 2230 CST and 0000 CST result from the cold air being advected over the relatively warm underlying surface. The evolution of the sensible heat flux is well in phase with the evolution of the virtual sensible flux but sensible heat flux is a little lower since the virtual sensible heat flux contains the contribution from the water vapour too.

4.2 Radiative Fluxes at Cloud Boundaries

In addition to the buoyancy fluxes generated at the surface, longwave radiative cooling at cloud top can generate turbulence. During the day the solar absorption at the top of the cloud can mediate some of the longwave radiative cooling and reduce the turbulence generation. To investigate the radiation field through the cloud layer we use the numerical procedure as implemented by Mather et al. (2007) to calculate longwave and shortwave fluxes and the associated radiative heating rates. These calculations are made with the radiative transfer model of Fu and Liou (1992). The updates to the model and the cloud (liquid and ice) radiative properties used in the model are described in Mather et al. (2007). The model output vertical resolution is 45 m in the cloud layer. The radiative transfer calculation was made every minute using the atmospheric profile from the ARM Merged Sounding value added product, the cloud properties from the Actively Remote Sensing of Clouds (ARSCL) value added

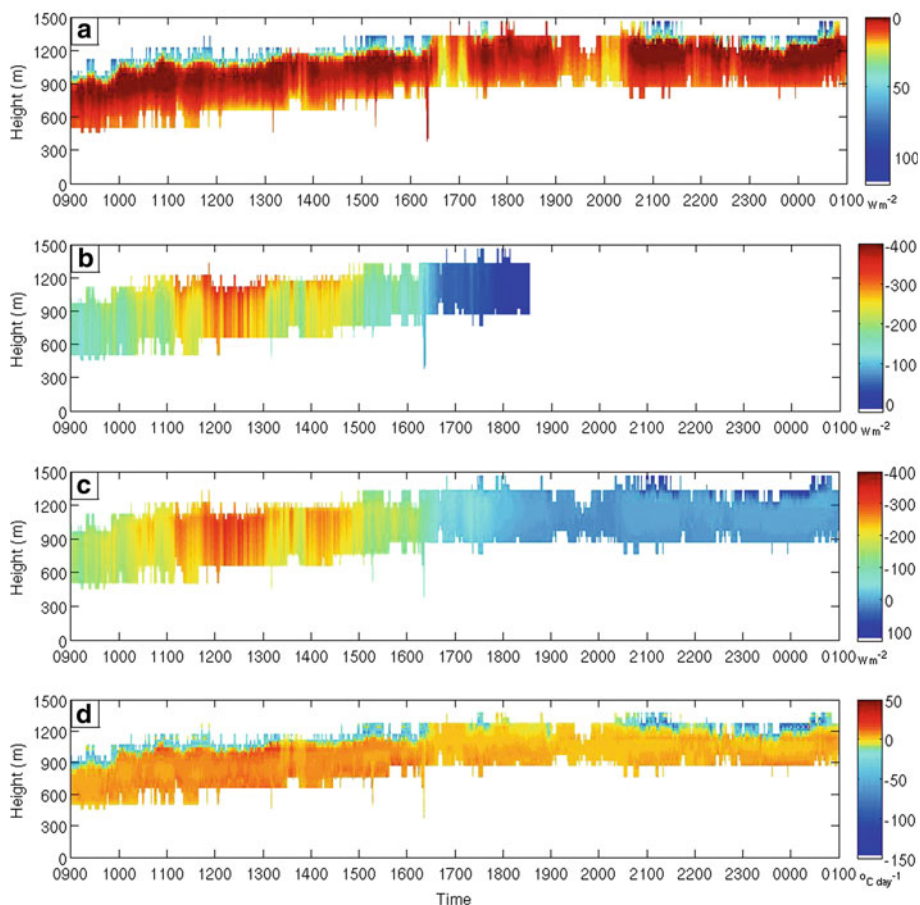


Fig. 4 The time-height display of, from *top to bottom*, net longwave radiative flux (a), net shortwave radiative flux (b), net radiative flux (c) and heating/cooling rate (d)

product, the LWP from the microwave radiometer, aerosol properties from the Aerosol Best Estimate value added product and the shortwave surface albedo from the MultiFilter Rotating Shadowband Radiometer. The vertical distribution of cloud liquid water content is obtained by using the ARSCL cloud boundaries and radar reflectivity profiles with the LWP as an integral constraint. The carbon dioxide mixing ratio was set at 360 ppmv, while the ozone properties were obtained from the total ozone mapping spectrometer.

Figure 4 shows the net longwave radiative flux, net shortwave radiative flux, net radiative flux and the heating/cooling rate in the cloud layer. A positive radiative flux indicates an outgoing flux, whereas a negative radiative flux indicates an incoming flux. The net longwave radiative flux is always slightly positive near cloud base. In the clouds, most values are close to zero. Compared with that around cloud base, the positive values at the cloud top are much higher except between 1630 CST and 1720 CST, 1740 CST and 2020 CST and the time period around 2200 CST. The upper-level clouds around 1700 CST and 2000 CST effectively reduce the longwave radiative flux at the cloud top and lead to two nearly constant flux streaks throughout the cloud layer. The net shortwave radiative flux is always negative

inside and around cloud layer, and larger negative values appear around noon when the solar radiation is the most intensive. The total net radiative flux is the sum of the net longwave flux and the net shortwave flux; it is negative during the day and slightly positive around cloud base and slightly negative or near zero inside clouds during the night. During the night, the large vertical gradient can be observed around the cloud top.

4.3 Time Evolution of Heating/Cooling Rate in Cloud Layer

The convergence/divergence of the net radiative flux or the heating/cooling rate can be related to the turbulence in the cloud layer. The heating/cooling rate is the time change rate of the temperature due to the flux divergence, and is calculated from

$$\left. \frac{\partial T}{\partial t} \right|_{\text{rad}} = -\frac{1}{\rho c_p} \frac{\partial F_{\text{net}}}{\partial z} \quad (1)$$

where $\rho = 1.21 \text{ kg m}^{-3}$ is the air density, c_p is the specific heat of moist air, F_{net} is the total net radiative flux, z is the height. From Fig. 4d it can be clearly seen that, on average, below the cloud top, the radiative flux convergence leads to heating of this part of the cloud layer. The heating is more prominent during the day than during the night and more prominent around cloud base than elsewhere at nighttime. Near cloud top, cooling is present except around 1330 CST, the time period between 1620 CST and 2020 CST and around 2200 CST when mid-level clouds pass over the site and the cloud-top cooling is significantly reduced or even shut-off. Further cloud-top cooling is present even during the day at the cloud top, although strong solar absorption occurs just below the cloud top and significantly mediates the cloud-top cooling around 1340 CST. The strongest cloud-top cooling is observed during nighttime when no upper-level clouds are present.

4.4 Time Evolution of Net Radiative Flux Difference

The time series of the calculated net radiative flux difference across the cloud layer ($F_{\text{net-ct}} - F_{\text{net-cb}}$) are shown in Fig. 5. The results in Fig. 5 are for the entire cloud layer whereas those shown in Fig. 4 are the detailed time-height plots. Positive (negative) values of ($F_{\text{net-ct}} - F_{\text{net-cb}}$) represent radiative flux divergence (convergence) within the cloud layer and lead to cloud-layer cooling (warming). From 0900 CST to 1620 CST the net radiative flux divergence is modulated by the impact of the solar radiation on the cloud layer directly by absorption and indirectly by warming of the surface. Around noon, ($F_{\text{net-ct}} - F_{\text{net-cb}}$) becomes positive, which signals that the net shortwave radiative flux slightly exceeds the net longwave radiative flux. The cloud-layer warming reaches a maximum around 1310 CST as upper-level clouds reduce the cooling of the cloud. Likewise, the net cooling in the cloud is diminished as the downwelling longwave radiation from the upper-level clouds offsets much of the outgoing radiation at cloud top as shown in Fig. 1 during periods between 1620 CST and 2050 CST and around 2200 CST. In Fig. 5, a double arrowed line combined with two vertical dotted lines indicates four time periods. Comparing with Fig. 1a, one can see that these time periods match well with the time periods of the mid-level mixed-phase cloud, which reflects that the mixed-phase cloud has a significant influence on the radiative flux budget at the low-level cloud top. The mid-level cloud influences on the net flux divergence are introduced by the inclusion of the Actively Remote Sensed Cloud value added product, which includes the radar observations shown in Fig. 1a. There are smaller clouds appearing around 2320 CST and 0100 CST. During the night when upper-level clouds are not present, the net radiative

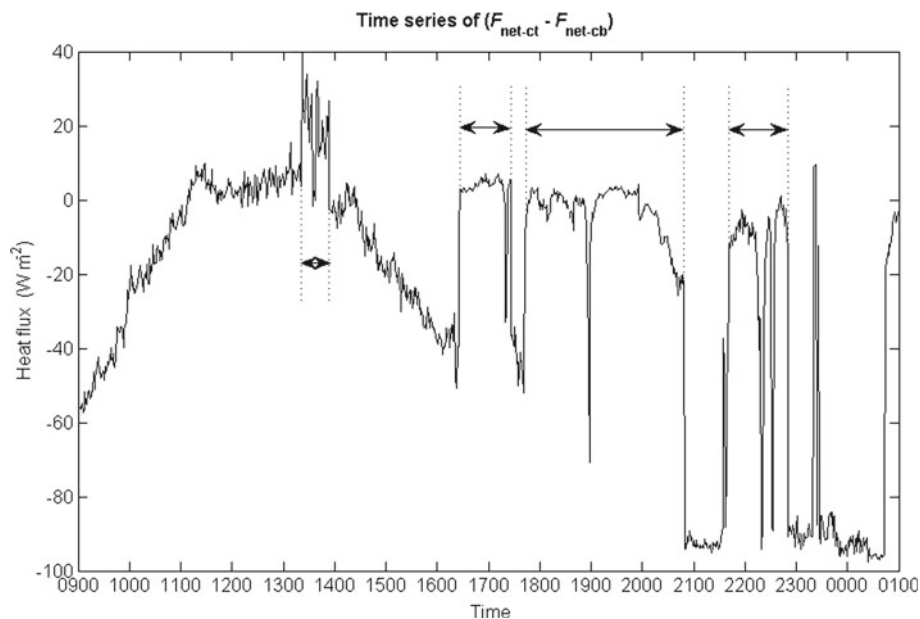


Fig. 5 The difference of the total net radiative flux between cloud top and cloud base from radiative transfer calculations. A double arrow line combined with two vertical dotted lines indicates a time period when midlevel clouds are observed over the site as shown in Fig. 1a

energy loss is a maximum and gives the relatively broader dips in $(F_{\text{net-ct}} - F_{\text{net-cb}})$ around 1730 CST, 2100 CST, 2300 CST and around midnight.

5 Convective and Radiative Velocity Scales

The convective velocity scale can be used as indicator of the external forcing due to buoyancy and an appropriate scaling of the turbulence intensity. For stratocumulus clouds the generalized convective velocity scale has been formulated as $W_*^3 = 2.5 (g/\theta) \int_0^h \overline{W'\theta_v'} dz$ following Deardorff (1980a). Nicholls (1984) used a simplified representation for W_* given as $W_*^3 = (g/\theta) (\overline{W'\theta_v'})_m d$ where $(\overline{W'\theta_v'})_m$ is the maximum flux at any point in the vertical profile and d is the depth of the boundary layer. Since both the generalized velocity scale and the Nicholls (1984) formulations require the vertical distribution of the buoyancy flux, it is difficult to apply to the observations used in this study. Further, for stratocumulus clouds the surface buoyancy fluxes can contribute substantially to the turbulence generation in combination with the cloud-top radiative cooling. Thus, here we follow the approach used by Lock and MacVean (1999a) and Ghate et al. (2012) and combine two velocity scales—the surface convective velocity scale and the radiative convective velocity scale. In addition to the surface heating and the cloud-top radiative cooling, the wind shear and the latent heating and cooling due to the change of water phase can also contribute to turbulence production (Lock 1998; Zhu et al. 2001; Mechem et al. 2010). However, we do not construct a universal velocity scale that takes all possible contributors into account and is applicable to every situation. Moreover, here, the shear is weak and negligible. Lock (1998) and Lock and MacVean (1999b) propose another velocity scale that includes the entrainment induced by a buoyancy

reversal driven by evaporative cooling as well as surface heating and cloud-top radiative cooling; but calculations from soundings show conditions (equivalent potential temperature increases across the inversion) that do not support a buoyancy reversal. Thus, this study will focus on surface heating and cloud-top cooling and assume that they are the only source of the turbulence.

The surface convective velocity scale is equivalent to the traditional convective velocity scale W_* (Deardorff 1980a) and the radiative convective velocity scale is that defined by Lock and MacVean (1999a) so that

$$W_s^* = \left[\frac{gz_t}{\theta_v} \left(\overline{W'\theta_v'} \right) \right]^{\frac{1}{3}}, \quad (2a)$$

$$W_r^* = \left[\frac{gz_t (-\Delta F_r)}{\theta_v \rho C_p} \right]^{\frac{1}{3}}, \quad (2b)$$

where $g = 9.8 \text{ m s}^{-2}$ is the acceleration due to gravity, z_t is the cloud-top height and ΔF_r is the net radiative flux divergence across the cloud layer as shown in Fig. 5. Following Lock and MacVean (1999a) we define the total convective velocity scale W_t^* as the cubic sum

$$W_t^{*3} = W_s^{*3} + W_r^{*3} \quad (2c)$$

where the surface forcing velocity scale W_s^* is calculated using the observed surface buoyancy fluxes and the radiative convective velocity scale W_r^* that is based on the flux divergence across the entire cloud layer. This formulation allows for the possibility that longwave radiative heating at cloud base can also contribute to the generation of turbulence.

The time variations of W_s^* , W_r^* and W_t^* for the case investigated here are shown in Fig. 6. W_s^* slightly increases from 0900 CST to 1300 CST as the surface warms by the solar radiation that is transmitted through the cloud and absorbed at the surface. The surface heating (and the surface buoyancy flux) decreases in the afternoon and reduces to zero after sunset. The peaks in W_s^* around midnight are due to cold air moving over a relatively warmer surface. In the free atmosphere above the boundary layer the geostrophic wind turns in a counterclockwise direction with height (backing winds as shown in Fig. 2b), that is consistent with cold-air advection. By checking the time series of the 24-h surface temperature difference, which is equal to the current temperature minus the temperature 24 h before and not shown here, one can see that the cold-air advection is strong during the day and is weakened but persistent during the night. These observations support our deductions. The radiative velocity scale decreases from 0900 CST when shortwave radiative heating tends to compensate longwave cloud-top cooling and reduces the radiative velocity scale to near zero around local noon when the shortwave radiation compensation reaches a maximum. After 1300 CST, the radiative velocity increases as the shortwave-induced cloud-layer heating decreases. The radiative velocity scale W_r^* is a maximum around midnight, but it is reduced around 1700 CST, 2000 CST and 2200 CST as the downward longwave radiation increases at cloud top as upper-level clouds move over the site. During the day, the total velocity scale is primarily attributed to the surface heating around noon and to both surface heating and cloud-top cooling in the morning and afternoon. During the night, the major contributor is the cloud-top radiative cooling, although Fig. 4d shows that the radiative warming at cloud base also contributes to W_r^* and is a substantial fraction of W_t^* when upper-level clouds are present. It will be shown later that these two well-defined forcing mechanisms provide a means to examine how the turbulence structure develops and varies between day and night respectively, and that the lower W_t^* values between 1800 CST and 2000 CST also explain the weaker turbulence during

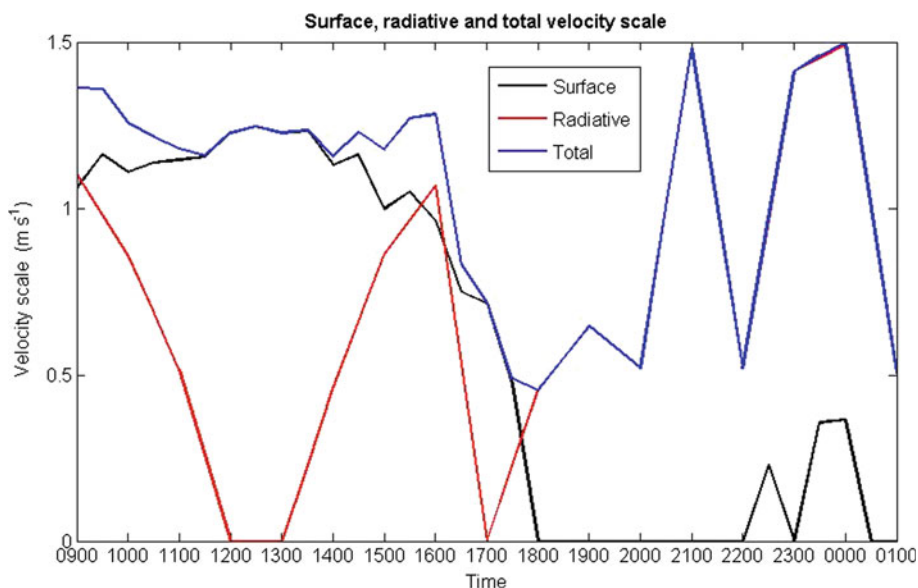


Fig. 6 Time series of the surface convective velocity scale, cloud-top radiative velocity scale and the total velocity scale

these times and provide an excellent opportunity to evaluate the response of the turbulence to changes in the forcing.

The averages of W_s^* , W_r^* and W_t^* from 0900 CST to 1800 CST are 1.05 m s^{-1} , 0.52 m s^{-1} and 1.15 m s^{-1} and from 1800 CST to 0100 CST are 0.09 m s^{-1} , 0.86 m s^{-1} and 0.88 m s^{-1} respectively. These values combined with Fig. 6 indicate that surface heating and cloud-top radiative cooling are equally important in determining the turbulence in the boundary-layer clouds during the day whereas cloud-top cooling is the exclusive contributor during the night, which differs from that in marine stratocumulus clouds where cloud-top cooling is always the major external forcing, although this cooling is reduced during the day by solar warming in the cloud.

6 Time Evolution of Variance, Squared Spectrum Width and Skewness

The Atmospheric Radiation Measurement program millimetre-wave cloud radar has a 4-s time resolution (Kollias et al. 2005). The high time resolution makes it possible to examine the temporal evolution of the vertical structures of the turbulence in detail. Figure 7 shows the time-height mapping of the radial velocity variance, i.e. $\sigma_{V_r}^2$, squared spectrum width (SSW) and skewness. All values shown in Fig. 7 are hourly values. To calculate $\sigma_{V_r}^2$ and skewness, the hourly mean of the radial velocity has been subtracted from each instantaneous measurement of that hour. SSW shown in Fig. 7 is an hourly median value; the ordinate is a normalized height that is defined as the height above cloud base normalized by cloud depth.

The variance of radial velocity is primarily due to resolved turbulence on scales larger than the radar resolution volume. Although it may not agree with W_t^* shown in Fig. 6 in detail, it is generally consistent with W_t^* . Since 0626 CST and 1846 CST are the times of sunrise and sunset respectively on 25 March 2005, from Fig. 7a one can see that the variance of radial

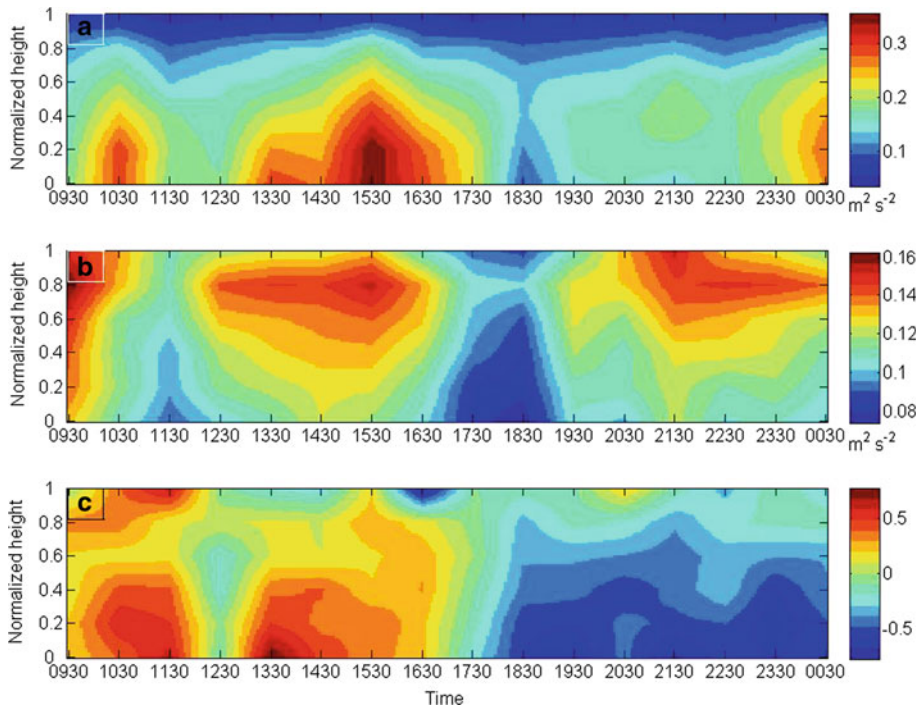


Fig. 7 Time-height display of the radial velocity variance (a), squared spectrum width (b) and skewness (c). The labels on the x-axis are not at the top of the hours since each displayed value is an hourly median

velocity roughly follows the diurnal cycle of the total velocity scale. As with W_t^* , $\sigma_{V_r}^2$ has two maxima during the day. One is around 1030 CST about 1 h lagged with the associated maximum W_t^* and W_r^* ; another is around 1530 CST appearing about 30 min earlier than the associated maximum W_t^* and W_r^* . It will be shown later that the 1-h lagged time is consistent with the response time of the turbulence in clouds to the external forcings. However, the 30-min advance time implies that the turbulence in clouds has a more complex relation with the convective and radiative forcings.

The radial velocity variance $\sigma_{V_r}^2$ is higher during the day than at night. This is opposite to the diurnal variation of the turbulence in marine stratocumulus clouds where the stronger turbulence appears during the night when cloud-top cooling is stronger (Frisch et al. 1995). The lowest values of $\sigma_{V_r}^2$ occur around sunset, when the radiative cooling is also small due to clouds above the low-level stratus, as shown in Fig. 6, that reduce the cloud-top radiative cooling. $\sigma_{V_r}^2$ increases after sunset when the upper-level clouds move away and the radiative cooling at cloud top increases. During the day, from cloud base to cloud top, $\sigma_{V_r}^2$ decreases with height, which is consistent with a surface-based forcing mechanism. In this case a spectrum of eddies of differing dimensions are forced by the surface heating. Since only the largest eddies will extend through the depth of the boundary layer, a maximum in the variance is observed near the middle of boundary layer. This structure is consistent with the variance profile observed in the dry boundary layer during the day over land. From around sunset to midnight, cloud-top cooling leads to another maximum of $\sigma_{V_r}^2$ around 0030 CST near cloud base where $\sigma_{V_r}^2$ also decreases with height. Since the decoupled mixed layer below the cloud base, which is due to the colder ground surface resulting in a deepening boundary layer, the

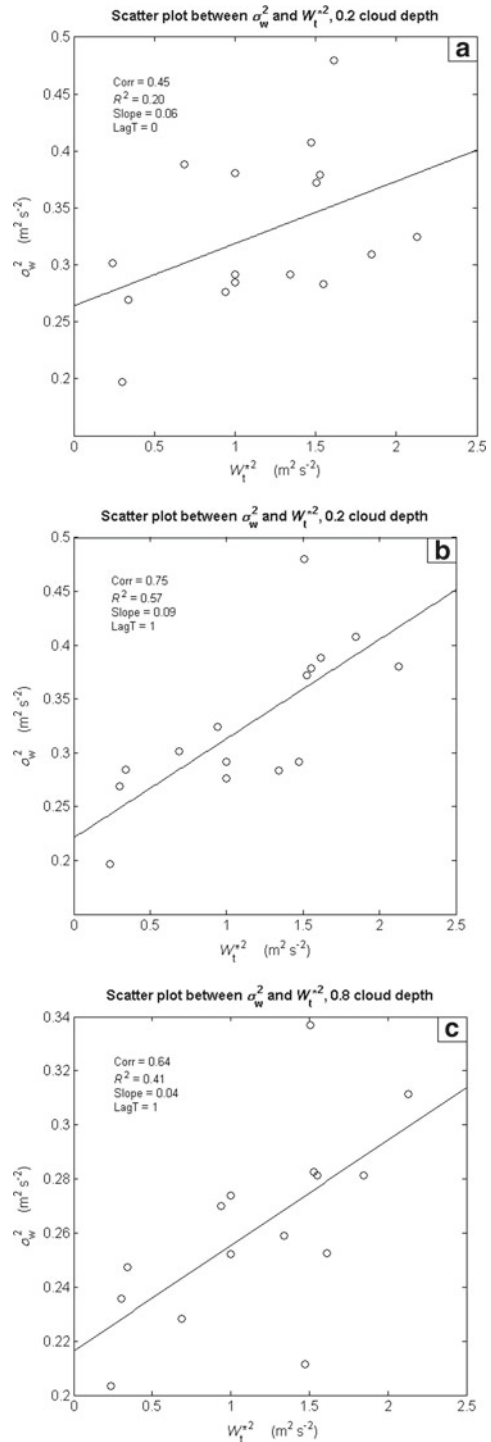
radiative cooling is the only external forcing driving the in-cloud turbulence. This vertical distribution of σ_{vr}^2 at night indicates that the cloud-top cooling creates relatively larger and stronger eddies at cloud base when cold air is sinking and accelerating due to the gravity.

The squared spectrum width or SSW is primarily due to the unresolved turbulence on scales comparable with and smaller than the radar beam size. It also follows the diurnal cycle. Two time periods of lowest values occur around noon and sunset when cloud-top cooling is reduced due to solar heating and longwave radiation from upper-level clouds respectively. In contrast to σ_{vr}^2 , the SSW increases with height with the maximum appearing around 0.8 times the normalized height at the base of the entrainment layer. This observation indicates that the unresolved turbulence more closely relates to the processes near cloud top.

The skewness of the millimetre-wave cloud radar measured Doppler velocity reflects the asymmetry of the vertical air motion distribution. Positive skewness indicates the presence of narrow width updrafts with stronger magnitude surrounded by wider areas of weak downdrafts and negative skewness indicates strong narrow downdrafts surrounded by large areas of weaker updraft (Moyer and Young 1991). Figure 7c demonstrates that positive skewness prevails during the day and negative skewness prevails at night. The transition occurs around 1730 CST when the convective velocity scale, i.e. W_s^* , sharply decreases as shown in Fig. 6. Similar results have been also reported by e.g. Nicholls (1984), Kollias and Albrecht (2000), Hogan et al. (2009), but here the millimetre-wave cloud radar with its high spatial resolution and continuous observations allows us to investigate the detailed evolution of the turbulence and the associated statistics. The results indicate that surface heating during the day creates strong narrow updrafts while the cloud-top cooling creates strong narrow downdrafts during the night. Although the radiative forcing across the entire cloud layer is positive around noon as shown in Fig. 5, the strong radiative cooling still exists at cloud top as shown in Fig. 4d. This might be the reason for the relative minimum of the skewness around 1230 CST. The inversion layer at cloud top resists and decelerates updrafts, and this deceleration results in a decrease of positive skewness with height. The acceleration of the sinking cloud air from cloud top is responsible for the increase in magnitude of negative skewness at lower heights in the cloud. This observation supports the previous deduction that the cloud-top cooling can drive larger scale turbulence near cloud base when cold air sinks and is accelerated by gravity.

To further investigate the relation between total velocity scale, i.e. W_t^* , and turbulence, Fig. 8a shows the scatter plot between total variance, i.e. σ_w^2 , and W_t^{*2} at the normalized height of 0.2. The correlation coefficient between the two variables is about 0.45, and in order to evaluate how good the linear regression is, R^2 is also calculated and displayed. The value of R^2 indicates the fraction of the variance that is explained by the regression model. It is 0.20, so that the linear model shown in Fig. 8a can only explain 20 % of the variance. Considering that a finite time is required for the air inside the cloud layer to response to the external forcings, we use the σ_w^2 that is lagged by 1 h with W_t^{*2} and show the results in Fig. 8b. Compared with those shown in Fig. 8a, the correlation and R^2 have substantially increased to 0.75 and 0.57 respectively, which indicates that the time for air in the cloud layer to respond to the external forcings is about 1 h. The higher correlation at cloud depth of 0.2 may also imply that the evaporation cooling below the cloud base or in the subcloud layer is negligible, which is consistent with the observation that beneath the cloud base no drizzle is detected. Figure 8c shows a result similar to that shown in Fig. 8b at a cloud depth of 0.8. Compared to that at a cloud depth of 0.2, the correlation and R^2 slightly decrease. Lock (1998) suggest that near cloud top the entrainment-induced evaporation reversal can also contribute to the turbulence generation, but no evaporation reversal exists for this case. However, the entrainment and the entrainment induced evaporation can damp turbulence by consuming

Fig. 8 The scatter plot between the total velocity scale W_t^{*2} and total variance σ_w^2 . **a**, **b** show results at the normalized height=0.2 whereas **c** has the normalized height=0.8. In **b** σ_w^2 is lagged by 1 h with W_t^{*2}



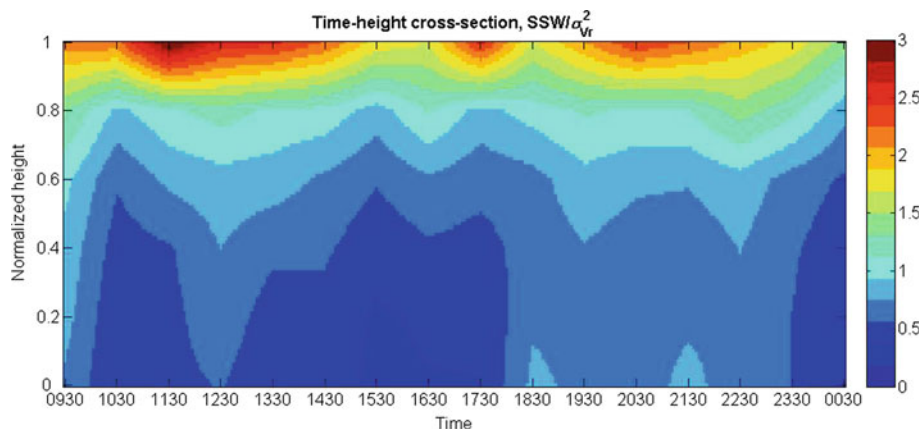


Fig. 9 Time-height display of the ratio between squared spectrum width and the variance of the vertical velocity

turbulent energy and reducing the instability near cloud top. The reduced correlation and the R^2 at cloud depth = 0.8 may reflect the fact that these damping effects are not included in the velocity scale W_t^* .

7 Resolved and Unresolved Turbulence

Rogers and Tripp (1964) proposed the Doppler radar-based energy partition theory for pure turbulent flow with zero mean velocity. This theory states that the total turbulence energy or velocity variance is partitioned into two parts: the first is the contribution from turbulence with scales larger than the radar beam size that is equal to the mean radial velocity variance; the second is the contribution from turbulence with scales smaller than radar beam size that is the variance of the expected Doppler spectrum or equal to the expected value of the squared spectrum width due to turbulence. Fang and Doviak (2008) extended this theory to the general flow with non-zero mean velocity. Based upon this theory, the resolved turbulence with scales larger than the radar beam size contributes to the variance shown in Fig. 7a, whereas unresolved turbulence with scales comparable with or smaller than radar beam size contributes to the SSW shown Fig. 7b. To examine the relative significance of the resolved and unresolved turbulence, Fig. 9 shows the time-height cross-section of the ratio between SSW and the variance of radial velocity. A magnitude of 1 indicates the locations where they are equal. It can be seen that unresolved turbulence dominates near the cloud top whereas resolved turbulence dominates almost elsewhere. The ratio below a cloud depth = 0.4 is higher at night than during the day, and is consistent with the fact that $\sigma_{V_r}^2$ is lower and SSW is higher during the night as shown in Fig. 7a, b. The lowest ratios appearing around 1100 CST, 1600 CST and 0030 CST can be attributed to the corresponding $\sigma_{V_r}^2$ peaks.

8 Summary

Observations are analyzed for a continental stratocumulus cloud layer capping the top of the boundary layer for over 16 consecutive hours. The cloud deck is observed in a region

of subsidence that occurs after a frontal passage and associated with an anticyclone located about 1,200 km north of the observation site. The large-scale background is similar to that commonly associated with marine stratocumulus clouds. However, the temporal evolution of the turbulence structure in this continental stratocumulus cloud is influenced by large variations in the surface energy fluxes and modulation of the cloud-top radiative cooling by solar absorption and variations in the downwelling longwave radiation at cloud top. The temporal variations in the turbulence forcings and the turbulence structures are studied using observations from a profiling cloud radar and supplemental instruments deployed in the Southern Great Plains site and a radiative transfer model that helps to characterize the temporal evolution of forcings in the boundary layer.

It has been shown that the radar-observed cloud depth changes with time and is consistent with the LWP observed by microwave radiometer. However, the diurnal cycle of the cloud thickness and LWP observed in marine stratocumulus clouds are not observed in these continental stratocumulus clouds. A reduction of the cloud depth around 1930 CST may be attributed to the existence of upper-level clouds that weaken the cloud-top cooling and the related turbulence that maintains the clouds. The sensible heat flux, virtual sensible heat flux, latent heat flux and the net radiative flux at the surface exhibit a diurnal cycle, increasing in the morning, reaching a maximum around noon and decreasing afterwards. During the night, virtual sensible heat and the net radiative flux reduce to about zero. Radiative transfer model results indicate that the strong radiative cooling around cloud top exists during the entire period investigated except during periods when upper-level clouds exist. Inside the cloud layer the radiative heating exists, but it is more prominent during the day due to solar absorption and more prominent near cloud base at night due to convergence of the longwave radiative fluxes.

Two convective velocity scales, i.e. W_s^* and W_r^* , are defined and combined to form the total velocity scale W_t^* that can be related to the in-cloud turbulence in the atmospheric boundary layer. The total velocity scale also effectively tracks the turbulence forcing due to both the surface buoyancy fluxes and that associated with the cooling at cloud top. The convective velocity scale shows a typical diurnal cycle; it is almost constant before 1430 CST and then decreases to zero around sunset. The radiative velocity scale has a phase opposite to the solar radiation and reflects the fact that the solar radiation weakens the radiative cooling occurring around cloud top. It decreases when the solar radiation intensity increases and increases when the solar radiation intensity decreases, reaching the maximum during the night. The radiative velocity scale also decreases when upper-level clouds exist and cloud-top cooling is weakened.

The calculated mean values of W_s^* , W_r^* and W_t^* for day and night indicate that both surface heating and cloud-top cooling are important in driving the boundary-layer turbulence during the day and cloud-top cooling is the exclusive cause during the night, which differs from the situation in marine stratocumulus cloud where cloud-top cooling is the dominant source of turbulence. The variability in the forcings or the sources of turbulent kinetic energy provides a useful way to track the evolution of the turbulence structure in the cloud.

The radial velocity variance, i.e. $\sigma_{V_r}^2$, follows the diurnal cycle and is consistent with the total velocity scale W_t^* . It has two maxima, and is higher during the day, and has one maximum and is lower during the night, which is contrary to that in the marine stratocumulus clouds where the turbulence is relatively stronger at night and weaker in the day. The lowest radial velocity variance occurs around sunset, when the radiative cooling is also small due to clouds above the low-level stratus. During the day, $\sigma_{V_r}^2$ decreases with height, which is consistent with a surface-based forcing mechanism; during the night when cloud-top cooling is the only mechanism to drive the turbulence, the $\sigma_{V_r}^2$ decreases with height also, which

implies that the cloud-top cooling creates the relatively larger scale turbulence near cloud base. The squared spectrum width also follows the diurnal cycle. Two time periods of lowest values occur around noon and sunset when cloud-top cooling is reduced due to solar heating and longwave radiation from upper-level clouds respectively. The vertical distribution of the squared spectrum width indicates that the unresolved turbulence more closely relates to processes near cloud top. Turbulence in cloud needs about 1 h to respond to the external forcings. The millimetre-wave cloud radar's capability of measuring both resolved and unresolved turbulence provides the possibilities to verify or test the approaches that are used in LES models to parametrize the subgrid processes.

It has been shown that positive skewness prevails in the day and negative skewness prevails at night with a sharp transition around sunset. The vertical distributions of the skewness at day and night reflect the updraft deceleration and downdraft acceleration respectively. Moreover, resolved turbulence dominates near cloud base whereas unresolved turbulence dominates near cloud top, which closely relates to the cloud-top cooling. In Part II of this study, profiles of the integral length scale show that the scales are smaller near cloud top and larger near cloud base, which is consistent with and supports results presented here.

This case study of turbulence in a continental stratocumulus cloud provides a unique description of the turbulence variations associated with hourly changes in the turbulence generation processes due to daytime heating of the surface, a reduction of the cloud-top cooling due to solar absorption, and a reduction of cloud-top cooling during times when clouds above the low-level stratus are observed. Traditional methods of characterizing turbulence using aircraft measurements do not allow characterizations of the time variability of the turbulence on time scales of hours. The observations from Atmospheric Radiation Measurement program used in this study allow for a detailed description of both the temporal variations in the turbulence and the processes that force the turbulence. We have outlined a method that can be used in future, and which provides a means of evaluating the time evolution of turbulence structures in LES forced by varying surface and cloud-top radiative forcings.

Acknowledgments This research was supported by the Office of Biological and Environmental Research of the U.S. Department of Energy under grant DE SC0000777 as part of the Atmospheric Radiation Measurement program Climate Research Facility.

References

- Boutle IA, Abel SJ (2012) Microphysical controls on the stratocumulus topped boundary-layer structure during VOCALS-Rex. *Atmos Chem Phys* 12:2849–2863
- Deardorff JW (1980a) Stratocumulus-capped mixed layers derived from a 3-dimensional model. *Boundary-Layer Meteorol* 18:495–527
- Dunn M, Johnson K, Jensen M (2011) The Microbase value-added product: a baseline retrieval of cloud microphysical properties. DOE/SC-ARM/TR-095, U. S. Department of Energy, Washington DC, p 34
- Duynkerke PG, Roode SRD, Zanten MCV, Calvo J, Cuxart J, Cheinet S, Chlond A, Grenier H, Jonker PJ, Köhler M, Lenderink G, Lewellen D, Lappen CL, Lock AP, Moeng CH, Müller F, Olmeda D, Piriou JM, Sánchez E, Sednev I (2004) Observations and numerical simulations of the diurnal cycle of the EUROCS stratocumulus case. *Q J R Meteorol Soc* 130:3269–3296
- East TWR, Marshall JS (1954) Turbulence in clouds as a factor in precipitation. *Q J R Meteorol Soc* 80:26–47
- Fang M, Doviak RJ (2008) Coupled contributions in the Doppler radar spectrum width equation. *J Atmos Oceanic Technol* 25:2245–2258
- Frisch AS, Lenschow DH, Fairall CW, Schubert WH, Gibson JS (1995) Doppler radar measurements of turbulence in marine stratiform cloud during ASTEX. *J Atmos Sci* 52:2800–2808
- Fu Q, Liou KN (1992) On the correlated k-distribution method for radiative transfer in non-homogeneous atmospheres. *J Atmos Sci* 49:2139–2156

- Ghate VP (2009) Turbulence and mass-transport in stratocumulus clouds. Dissertation, University of Miami, 124 pp
- Ghate VP, Albrecht BA, Kollias P (2010) Vertical velocity structure of non-precipitating continental boundary-layer stratocumulus clouds. *J Geophys Res* 115:D13204. doi:[10.1029/2009JD013091](https://doi.org/10.1029/2009JD013091)
- Ghate VP, Albrecht BA, Miller MA, Brewer A, Fairall CW (2013) Turbulence and radiation in stratocumulus topped marine boundary layer: a case-study from VOCALS-Rex. *J Appl Meteorol Climatol*. doi:[10.1175/JAMC-D-12-0225.1](https://doi.org/10.1175/JAMC-D-12-0225.1)
- Hogan RJ, Grant ALM, Illingworth AJ, Pearson GN, O'Connor EJ (2009) Vertical velocity variance and skewness in clear and cloud-topped boundary layers as revealed by Doppler lidar. *Q J R Meteorol Soc* 135:635–643
- Jonas PR (1996) Turbulence and cloud microphysics. *Atmos Res* 40:283–306
- Kollias P, Albrecht BA (2000) The turbulence structure in a continental stratocumulus cloud from millimetre-wavelength radar observations. *J Atmos Sci* 57:2417–2434
- Kollias P, Albrecht BA, Lhermitte R, Savtchenko A (2001) Radar observations of updrafts, downdrafts, and turbulence in fair-weather cumuli. *J Atmos Sci* 58:1750–1766
- Kollias P, Jo I, Albrecht BA (2005) High-resolution observations of mammatus in tropical anvils. *Mon Weather Rev* 133:2105–2112
- Kollias P, Miller MA, Luke EP, Johnson KL, Clothiaux EE, Moran KP, Widener KB, Albrecht BA (2007) The atmospheric radiation measurement program cloud profiling radars: second-generation sampling strategies, processing, and cloud data products. *J Atmos Oceanic Technol* 24:1199–1214
- Lilly D (1968) Models of cloud-topped mixed layers under a strong inversion. *Q J R Meteorol Soc* 94:292–309
- Lock AP (1998) The parametrization of entrainment in cloudy boundary layers. *Q J R Meteorol Soc* 124:2729–2753
- Lock AP, MacVean MK (1999a) The parametrization of entrainment driven by surface heating and cloud-top cooling. *Q J R Meteorol Soc* 125:271–299
- Lock AP, MacVean MK (1999b) The generation of turbulence and entrainment by buoyancy reversal. *Q J R Meteorol Soc* 125:1017–1038
- Mather JH, McFarlane SA, Miller MA, Johnson KL (2007) Cloud properties and associated radiative heating rates in the tropical western Pacific. *J Geophys Res* 112:D05201. doi:[10.1029/2006JD007555](https://doi.org/10.1029/2006JD007555)
- Mechem DB, Kogan YL, Schultz DM (2010) Large-eddy observation of post-cold-frontal continental stratocumulus. *J Atmos Sci* 67:3368–3383
- Moran KP, Martner BE, Post MJ, Kropfli RA, Welsh DC, Widener KB (1998) An unattended cloud-profiling radar for use in climate research. *Bull Am Meteorol Soc* 79:443–455
- Moyer KA, Young GS (1991) Observations of vertical velocity skewness within the marine stratocumulus-topped boundary layer. *J Atmos Sci* 48:403–410
- Nicholls S (1984) The dynamics of stratocumulus: aircraft observations and comparisons with a mixed layer model. *Q J R Meteorol Soc* 110:783–820
- Rogers RR, Tripp BR (1964) Some radar measurements of turbulence in snow. *J Appl Meteorol* 13:603–610
- Sassen K, Mace GG, Wang Z, Poellot MR, Sekelsky SM, McIntosh RE (1999) Continental stratus clouds: a case study using coordinated remote sensing and aircraft measurements. *J Atmos Sci* 56:2345–2358
- Simon PDS, Yuter S, Mechem D, Fairall CW, Burleyson CD, Zuidema P (2012) Observations of stratocumulus clouds and their effect on the eastern Pacific surface heat budget along 20°S. *J Clim* 25:8542–8567
- Turner DD, Clough SA, Liljegren JC, Clothiaux EE, Cady-Pereira K, Gaustad KL (2007) Retrieving liquid water path and precipitable water vapour from Atmospheric Radiation Measurement microwave radiometers. *IEEE Trans Geosci Remote Sens* 45:3680–3690
- Wang LP, Grabowski WW (2009) The role of air turbulence in warm rain initiation. *Atmos Sci Lett* 10:1–8
- Wood R (2012) Stratocumulus clouds. *Mon Weather Rev* 140:2373–2423
- Wood R, Bretherton CS, Hartmann DL (2002) Diurnal cycle of liquid water path over the subtropical and tropical oceans. *Geophys Res Lett* 29:7-1–7-4.
- Xue Y, Wang L, Grabowski W (2008) Growth of cloud droplets by turbulent collision-coalescence. *J Atmos Sci* 65:331–356
- Zhu P, Albrecht BA, Gottschalk J (2001) Formation and development of nocturnal boundary-layer clouds over the Southern Great Plains. *J Atmos Sci* 58:1409–1426
- Zhu P, Albrecht BA, Ghate VP, Zhu Z (2010) Multiple scale simulations of stratocumulus clouds. *J Geophys Res* 115:D23201. doi:[10.1029/2010JD014400](https://doi.org/10.1029/2010JD014400)